



Nanocrystals of a new complex perovskite dielectric $\text{Ba}_2\text{TmSbO}_6$

V.M. Nair^a, R. Jose^{b,*}, G.M. Anil Kumar^c, Mashitah M. Yusoff^b, P.R.S. Warier^a

^a Department of Physics, University College, Trivandrum 695034, Kerala, India

^b Faculty of Industrial Sciences and Technology, Universiti Malaysia Pahang, 26300 Kuantan, Malaysia

^c Noritake Co Ltd, 300 Higashiyama, Miyoshi, Aichi 470-0293, Japan

ARTICLE INFO

Article history:

Received 24 June 2011

Received in revised form

19 September 2011

Accepted 20 September 2011

Available online 28 September 2011

Keywords:

Nanocrystals

Dielectric

Barium rare-earth antimonates

Crystal structure

Rietveld analysis

ABSTRACT

Nanocrystals of a new complex perovskites ceramic oxide, barium thulium antimony oxide – $\text{Ba}_2\text{TmSbO}_6$, were synthesized using a single step auto-ignition combustion process. The combustion product was single phase and composed of aggregates of nanocrystals of sizes in the range 20–50 nm. $\text{Ba}_2\text{TmSbO}_6$ crystallized in cubic perovskite structure with lattice parameter, $a = 8.4101 \text{ \AA}$. The polycrystalline fluffy combustion product was sintered to high density (~97%) at ~1450 °C for 4 h. Resistivity of the sintered specimen was ~5 MΩ/cm. The $\text{Ba}_2\text{TmSbO}_6$ has dielectric constant (ϵ') and dielectric loss ($\tan \delta$) of 17 and ~10^{−4} at 5 MHz; the new material would probably be developed as a low-loss dielectric material.

© 2011 Elsevier B.V. All rights reserved.

* Corresponding author. Tel.: +60 95492451; fax: +60 95492766.

E-mail addresses: rjose@ump.edu.my, joserajan@gmail.com (R. Jose).

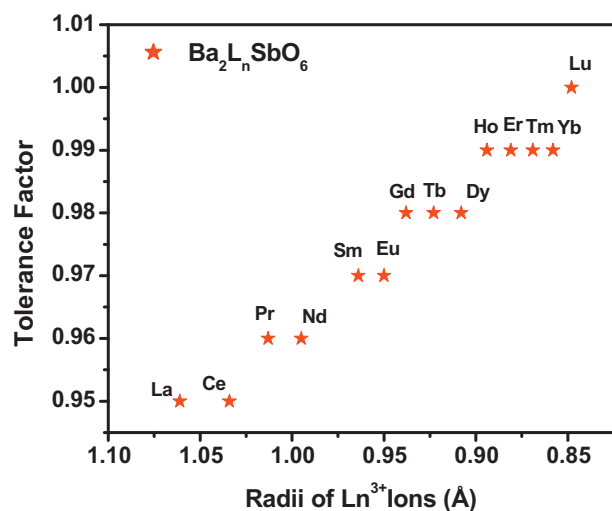


Fig. 1. Tolerance factor of $\text{Ba}_2\text{LnSbO}_6$ as a function of ionic radii of lanthanides. All the ionic radii were obtained from Shannon and Prewitt. The R_B was obtained from the average of radii of Ln and Sb.

To the best of our knowledge, little study was undertaken either on crystal structure or on dielectric properties for $\text{Ba}_2\text{LnSbO}_6$ that employs an Ln of lower ionic radii such as Tm. We have now synthesized $\text{Ba}_2\text{TmSbO}_6$ ($R_{\text{Tm}} < R_{\text{Ho}}$) as nanocrystals using a solution combustion method [14] and studied its crystal structure and dielectric properties. Synthesis of advanced and specialty materials as nanocrystals through wet chemical processes is recently a topic of intense research interest due to their characteristics such as superior phase purity, homogeneity, and sinterability which lead to compact solids with superior physical properties [15]. The $\text{Ba}_2\text{TmSbO}_6$ thus synthesized have cubic ($Fm\bar{3}m$) crystal structure as predicted by Fig. 1 and showed the lowest dielectric loss ($\tan \delta$) so far reported for any $\text{Ba}_2\text{LnSbO}_6$.

2. Experimental details

An aqueous solution containing ions of Tm, Ba, and Sb was prepared from high purity Tm_2O_3 (99.9%, Alfa Aesar, USA), $\text{Ba}(\text{NO}_3)_2$ (99.9%, CDH, India) and Sb_2O_3 (99.9%, Merck, USA) using the procedure described elsewhere [14–18]. The Tm_2O_3 and Sb_2O_3 were dissolved in nitric and tartaric acids, respectively. Citric acid was added to the solution containing the metal ions, maintaining the citric acid to the cation ratio at unity, to get a precursor complex. The oxidant fuel ratio of the system was adjusted by using nitric acid and ammonium hydroxide, and the ratio was kept at unity. The solution containing the complex precursor mixture at a pH of ~ 7.0 was heated using a hot plate at $\sim 250^\circ\text{C}$ in a ventilated fume-hood. The solution boils on heating and undergoes dehydration and decomposition leading to a smooth deflation and foams. The foam then ignites by itself on persistent heating giving voluminous and fluffy product of combustion. The as-prepared $\text{Ba}_2\text{TmSbO}_6$ were mixed with 5% polyvinyl alcohol, dried, and pressed in the form of cylindrical pellet of ~ 14 mm diameter and ~ 2 mm thickness at a pressure ~ 350 MPa. The pellets were then sintered at 1450°C for 4 h.

Crystal structure of the as-prepared powder and the sintered product were examined by powder X-ray diffraction (XRD) technique using X-ray diffractometer (Model Bruker D-8) with Nickel filtered $\text{Cu K}\alpha$ radiation. The differential thermal (DTA) and thermo gravimetric analyses (TGA) of the combustion product were carried out using Perkin-Elmer TG/DT thermal analyzer in the range 30 – 1000°C at a heating rate of $20^\circ\text{C}/\text{min}$ in nitrogen atmosphere. The infrared (IR) spectra of the samples were recorded in the range

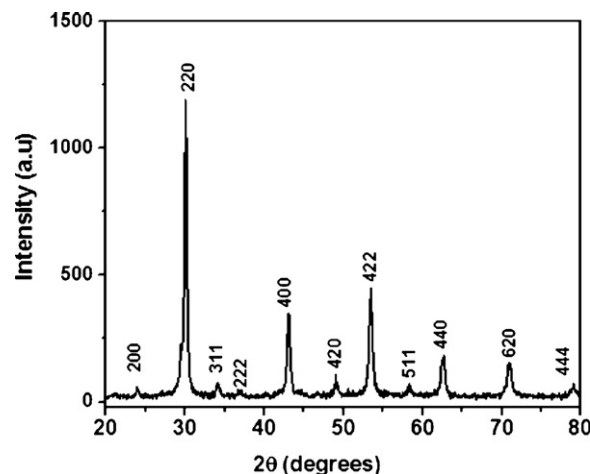


Fig. 2. XRD pattern of as-prepared $\text{Ba}_2\text{TmSbO}_6$ indexed to the (hkl) $Fm\bar{3}m$ space group.

400 – 4000 cm^{-1} on Thermo-Nicolet Avatar 370 Fourier Transform Infrared (FT-IR) spectrometer using KBr pellet method. Particulate properties of the combustion product were examined using scanning electron microscopy (SEM; Quanta 200 FEG System: FEI Company, USA) and transmission electron microscopy (TEM, Model-Hitachi H-600 Japan, 200 kV). Theoretical density of the $\text{Ba}_2\text{TmSbO}_6$ was calculated from the lattice constants and sintered density was measured following the Archimedes method. The surface morphology of the sintered samples was examined using SEM (Model-Hitachi S 2400, Japan). Crystal structure of the sintered material was studied by the Rietveld analysis of XRD measurements. PowderCell 2.3 program was used to fit the observed XRD patterns. For dielectric measurements, silver electrodes were attached on either sides of the sintered pellet and dried at 80°C for 15 min. The capacitance measurements were carried out using an LCR meter (HIOKI 3532-50) in the 50 Hz to 5 MHz frequency range.

3. Results and discussion

3.1. Powder characteristics and sintering of $\text{Ba}_2\text{TmSbO}_6$

The solution combustion process employing citric acid with the help of the ammonium hydroxide and nitrate ions [14] is currently the only available technique that synthesizes nanocrystalline metal oxides in a single step process. Usually powders obtained directly after combustion using this process are single phase; any further heating procedure only results in grain growth. Fig. 2 shows the XRD pattern of the as-prepared sample. No secondary or unreacted components were detected in the XRD patterns. All peaks in the XRD pattern were indexed for a cubic perovskite structure in Fig. 1. Lattice parameter calculated from the XRD pattern was $a = 8.409\text{ Å}$. Size of the crystallites calculated from the width of the XRD pattern was ~ 20 nm. Fig. 3 shows DTA and TGA curves of the powders after the combustion synthesis. The TGA curve did not show any appreciable weight change up to 1000°C indicating that the combustion is complete and there are no nitrates or carbonates; and therefore, the product is pure oxide. This observation was supported by DTA, which did not show any exothermic or endothermic peaks.

Fig. 4 displays the morphology and microstructures of the combustion product. Fig. 4A is a typical SEM image of the as-prepared powder, showing aggregates of uniform size. Fig. 4B is a TEM bright field image of a typical powder particle. The aggregates in terms consists of finer nanocrystallites of size ~ 10 – 20 nm. Fig. 4C shows a selected area electron diffraction (SAED) pattern recorded at an accelerating voltage of 200 kV, which corresponds to an electron

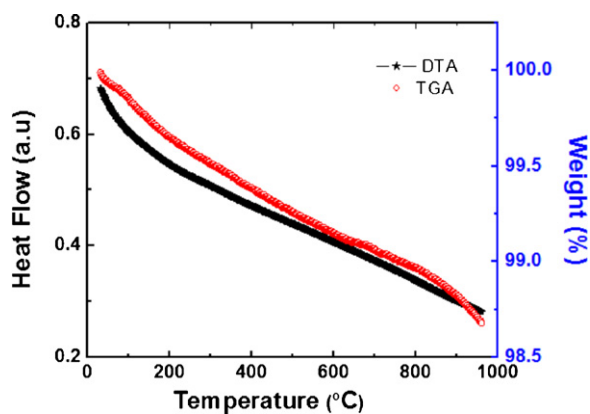


Fig. 3. DTA and TGA curves of the as-prepared $\text{Ba}_2\text{TmSbO}_6$.

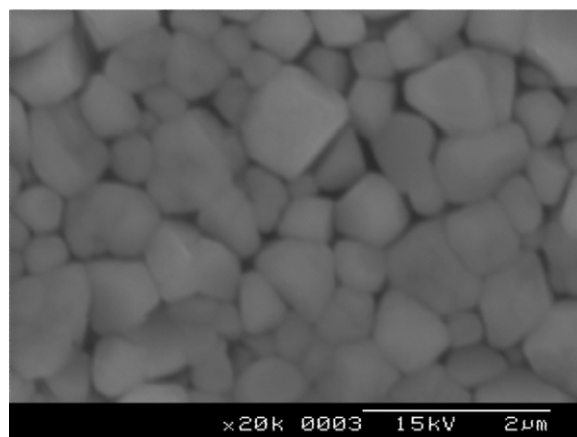


Fig. 5. SEM image of the sintered $\text{Ba}_2\text{TmSbO}_6$.

wavelength of 2.508 nm, and at a camera length of 915 mm. The SAED pattern shows rings that can be indexed to cubic structure. The ring nature of the SAED is indicative of the polycrystalline nature of the crystallites. Fig. 4D shows a high resolution lattice image showing a grain boundary; the grain boundary was sharp and free from any impurities.

The material was sintered and had high mechanical strength. The samples could be sliced into thin discs using a diamond cutter; well polished surfaces were obtained by mechanical polishing. Fig. 5 shows the surface morphology of the sintered $\text{Ba}_2\text{TmSbO}_6$ samples showing well crystallized sub-micron grains with sharp grain boundaries. No cracks or pores were observed on the surface. Sintering increased the grain size of the as-prepared $\text{Ba}_2\text{TmSbO}_6$; average grain size determined from the SEM micrographs was ~ 700 nm.

3.2. Structural characterization of $\text{Ba}_2\text{TmSbO}_6$

Fig. 6 shows the FT-IR spectrum of as-prepared $\text{Ba}_2\text{TmSbO}_6$ powder. The asymmetric stretching and bending modes of the BO_6 octahedra of the ABO_3 unit cell usually dominate the IR spectra of perovskites [16,19]. However, from a comparative study of the vibrational patterns of phonon modes in two types ABO_3 unit cells, Sopracase et al. concluded that most of phonon modes in these types of unit cells correspond to complex atomic vibrations and significantly different from one another which cannot be assigned only to a given type of vibration, i.e., external, bending, or stretching modes [20]. The present $\text{Ba}_2\text{TmSbO}_6$ (Ba_2LnMO_6) consists of corner-sharing SbO_6 (MO_6) and TmO_6 (LnO_6) octahedra. The band centred at $\sim 470\text{ cm}^{-1}$ is assigned to the asymmetric bending mode ν_4 (T_{1u}) of the SbO_6 (TmO_6) octahedra. The intense band centred at $\sim 620\text{ cm}^{-1}$ is assigned to the asymmetric stretching

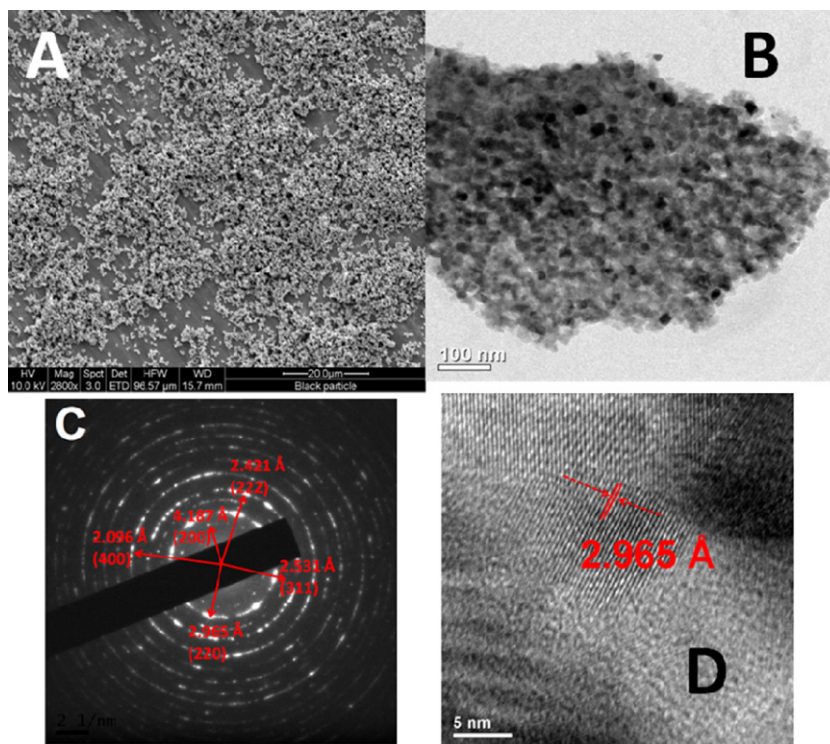


Fig. 4. (A) SEM image of the finely dispersed powder in ethanol; (B) bright field TEM image showing a typical powder particle; (C) selected area electron diffraction pattern of $\text{Ba}_2\text{TmSbO}_6$, the first five rings are indexed following the lattice parameter and camera constant; (D) a high resolution lattice image showing sharp grain boundary indicating the chemical purity of the material synthesized in the present work; the lattice fringe is from the (2 2 0) plane.

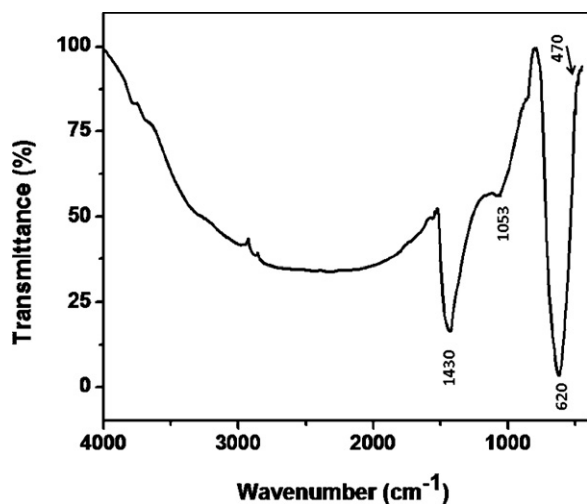


Fig. 6. FT-IR spectrum of $\text{Ba}_2\text{TmSbO}_6$. Refer the text for band assignments.

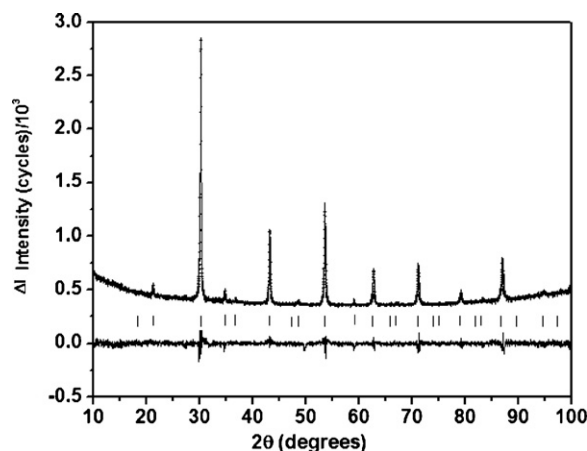


Fig. 7. Rietveld refinement plot of sintered $\text{Ba}_2\text{TmSbO}_6$. The black plus signs and the continuous lines show the experimental (I_{obs}) and simulated (I_{cal}) intensities, respectively. $\Delta I = I_{\text{cal}} - I_{\text{obs}}$ below. The vertical lines indicate positions of all the Bragg reflections from the $Fm\bar{3}m$ space group with lattice parameter 8.4101 Å.

mode ν_3 (T_{1u}) of the SbO_6 (TmO_6) octahedra. All these four bands merged into a single Gaussian profile indicating the similarity of bending/stretching frequencies of the SbO_6 and TmO_6 octahedra. Similar spectral pattern with two strong and well-defined IR bands in the $400\text{--}650\text{ cm}^{-1}$ region has been found in a number of Ba_2LnMO_6 perovskite type materials [21–24]. The weak band centred at 1053 cm^{-1} is assigned to the symmetric stretching mode ν_1 (A_{1g}) of SbO_6 (TmO_6) octahedra. The broad band centred at 1430 cm^{-1} arises from water vapour adsorbed due to ultrafine particle size of the combustion product. Similarity in the asymmetric and symmetric bending frequencies indicates that a symmetry lowering from cubic has not taken place in $\text{Ba}_2\text{TmSbO}_6$. We also note that the above observations corroborate the XRD and thermal analyses results that the combustion is complete and no organic matter present in the as-obtained combustion product.

Structure of the sintered $\text{Ba}_2\text{TmSbO}_6$ was studied by Rietveld analysis of X-ray diffraction measurements. Fig. 7 shows XRD patterns of the $\text{Ba}_2\text{TmSbO}_6$ and refined using the PowderCell 2.3 program [25]. Residues of fitting were $R_{\text{WP}}=4.13$, $R_p=3.12$, $R_e=3.13$, where the symbols have their usual meanings [25]. The goodness of fit indicator, $S=R_{\text{WP}}/R_e$, was 1.32, which represents a good fit. The lattice parameter of the sintered $\text{Ba}_2\text{TmSbO}_6$ was 8.4101 Å, very similar to that calculated from the XRD pattern of the as-prepared nanocrystals. All the peaks in the XRD pattern fit

well to cubic perovskite with space group $Fm\bar{3}m$ (No. 225). This space group allows two crystallographically distinct octahedral sites in $\text{Ba}_2\text{TmSbO}_6$ material, thus permitting the 1:1 positional ordering between B-site Tm^{3+} ions and Sb^{5+} ions. The ions are arranging alternatively and have a rocksalt sublattice. The alternative arrangement of Tm^{3+} and Sb^{5+} ions results in a superstructure. The Sb and Ln cations arrange randomly in equivalent positions of the crystal structure in a substitutional solid solution. If upon suitable heat treatment the random solid solution rearranges into a structure in which the Sb and Ln cations occupy the same set of positions but in a regular way, the structure is described as a superstructure. Presence of (odd, odd, odd) reflections such as (3 1 1) and (5 1 1) in the XRD patterns indicate the formation of the superstructure which lead to multiplication of the basic perovskite unit cell. Note that these reflections are also used to characterize the antiphase tilting occurs when $0.964 < t < 0.985$ [26]. However, t of the $\text{Ba}_2\text{TmSbO}_6$ is 0.992 which is expected to be an untilted system, as clearly demonstrated by the IR and XRD studies; and therefore, those reflections denote the superstructural doubling of the basic perovskite unit cell. Volume of the cell calculated from the cell parameters was 594.844 Å^3 . The theoretical density of $\text{Ba}_2\text{TmSbO}_6$ calculated from the cell volume and masses of the atoms composing the unit cell was 7.340 g/cm^3 . Sintered density of $\text{Ba}_2\text{TmSbO}_6$ was 7.08 g/cm^3 ; which was about $\sim 97\%$ of the theoretical density calculated from the XRD analysis.

To check whether any symmetry lowering than $Fm\bar{3}m$ was occurred in $\text{Ba}_2\text{TmSbO}_6$, the observed XRD pattern was fitted to the monoclinic $P2_1/n$ space group using the structural model described before [8]. Although the pattern fits well to the $P2_1/n$ space group also the residues were much higher than that of the $Fm\bar{3}m$ (S over 1.5). Therefore, within the limitations of the present experiment as well as predicted by Fig. 1, we conclude that $\text{Ba}_2\text{TmSbO}_6$ adopts cubic structure.

3.3. Dielectric properties of $\text{Ba}_2\text{TmSbO}_6$

The new material is an insulator with resistivity $\sim 5\text{ M}\Omega/\text{cm}$. The dielectric constant (ϵ_r) and loss factor ($\tan \delta$) of the new material were studied from capacitance measurements by sandwiching the sintered specimen between two silver electrodes. Fig. 8A shows the variation of ϵ_r and $\tan \delta$ as a function of frequency of the new material. The $\text{Ba}_2\text{TmSbO}_6$ has a ϵ_r of 17 and $\tan \delta$ of 10^{-4} at 5 MHz and at room temperature. The dielectric constant of a material can be calculated using the molar volume (V_m) and total dielectric polarizability (α_p) using the equation $\epsilon_r = ((3V_m + 8\pi\alpha)/3V_m - 4\pi\alpha)$. By using the dielectric polarizabilities reported by Shannon [27], we arrive at $\epsilon_r \sim 15.98$, which closely matches with the experimental value. The ϵ_r of the $\text{Ba}_2\text{TmSbO}_6$ was in a range reported for the other $\text{Ba}_2\text{LnSbO}_6$ (Fig. 8B) compiled from published literature [9]. The dielectric constant of the new material is in the medium range among the other $\text{Ba}_2\text{LnSbO}_6$ perovskites. However, the measured dielectric loss, i.e., $\tan \delta$, of the nanocrystalline $\text{Ba}_2\text{TmSbO}_6$ is the lowest among them. The $\tan \delta$ generally increases with increase in ϵ' , which arise from dielectric polarization. A possible source of discrepancy is the method of synthesis between the other rare-earth barium antimonates, whose microcrystals with lesser chemical purity were synthesized by the solid state reaction of oxides and/or carbonates. On the other hand, the present $\text{Ba}_2\text{TmSbO}_6$ is nanocrystalline with superior chemical purity due to atomic level mixing of the ions forming the compound. The lower value of $\tan \delta$ for a higher ϵ' is thus expected to arise from the chemical purity as well as submicron sized grains in the sintered product. The lower $\tan \delta$ of the new material is beneficial to fabricate low-loss microwave electronic circuits.

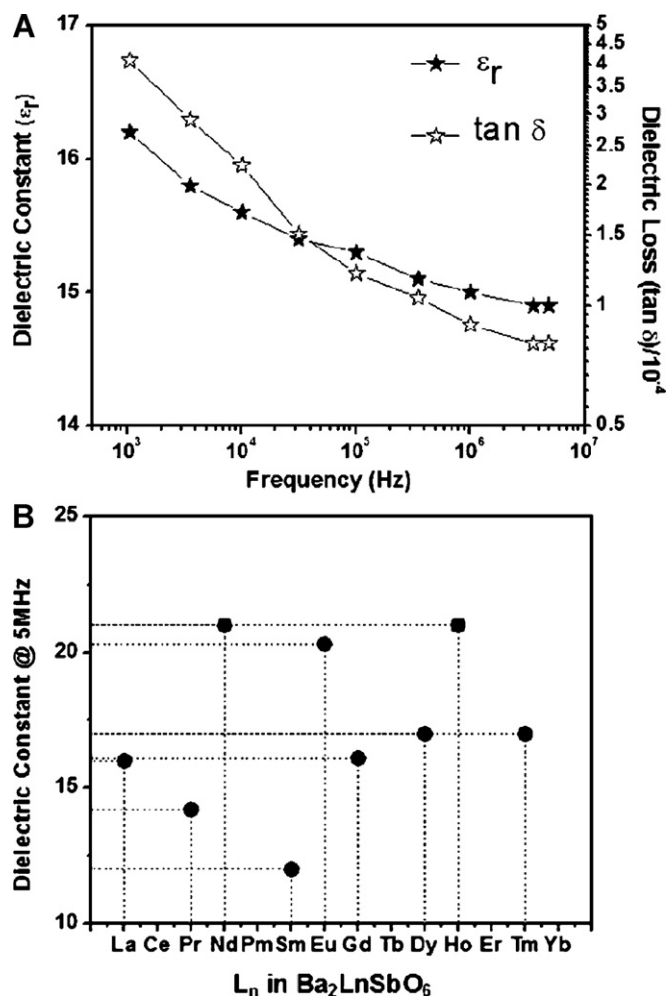


Fig. 8. (A) Dielectric constant and loss factor of $\text{Ba}_2\text{TmSbO}_6$ determined from the capacitance measurements and (B) the dielectric constant of sintered $\text{Ba}_2\text{LnSbO}_6$ determined from the published literature.

4. Conclusions

In conclusion, a new material $\text{Ba}_2\text{TmSbO}_6$ has been synthesized as single phase nanoparticles of average size 30 nm using a

combustion process. X-ray diffraction and electron diffraction have shown that the as-prepared powder is single phase $\text{Ba}_2\text{TmSbO}_6$ and has a complex perovskite structure with lattice constant $a = 8.4101 \text{ \AA}$. The nanocrystalline $\text{Ba}_2\text{TmSbO}_6$ was sintered to ~97% of its theoretical density at 1450°C for 4 h with well faceted cuboidal morphology. The $\text{Ba}_2\text{TmSbO}_6$ is an insulator (resistivity $\sim 5 \text{ M}\Omega/\text{cm}$) and has dielectric constant (ϵ') and dielectric loss ($\tan \delta$) of ~ 17 and $\sim 10^{-4}$ at 5 MHz, respectively. The new material was featured by a lowest dielectric loss among the other barium rare-earth antimonates.

References

- [1] N. Biskup, M. García-Hernández, I. Álvarez-Serrano, M.L. López, M.L. Veiga, J. Alloys Compd. 509 (2011) 4917.
- [2] A. Chronos, R.V. Vovk, I.L. Goulatis, L.I. Goulatis, J. Alloys Compd. 494 (2010) 190.
- [3] M. Mochizuki, N. Furukawa, N. Nagaosa, Phys. Rev. Lett. 105 (2010) 037205.
- [4] L. Shi, F. Bai, J. Chinese Ceram. Soc. 39 (2011) 550.
- [5] P.J. Saines, B.J. Kennedy, J. Solid State Chem. 181 (2008) 298.
- [6] W.T. Fu, S. Akerboom, D.J.W. Ijdo, J. Alloys Compd. 476 (2009) L11.
- [7] P.J. Saines, B.J. Kennedy, M.M. Elcombe, J. Solid State Chem. 180 (2007) 401.
- [8] R. Jose, J. Konopka, X. Yang, A. Konopka, M. Ishikawa, J. Koshy, Appl. Phys. A 79 (2004) 2041–2047.
- [9] J. Kurian, J. Koshy, P.R.S. Wariar, Y.P. Yadava, A.D. Damodaran, J. Solid State Chem. 116 (1995) 193.
- [10] Y. Markendeya, D. Saritha, M. Vithal, A.K. Singh, G. Bhikshamaiah, J. Alloys Compd. 509 (2011) 5195.
- [11] R.D. Shannon, C.T. Prewitt, Acta Crystallogr. B 25 (1969) 925.
- [12] W.T. Fu, D.J.W. Ijdo, J. Solid State Chem. 178 (2005) 2363.
- [13] J.A. Alonso, C. Cascales, P. García Casado, I. Rasines, J. Solid State Chem. 128 (1997) 247.
- [14] R. Jose, A.M. John, J.K. Thomas, J. James, J. Koshy, R. Divakar, E. Mohandas, Mater. Res. Bull. 42 (2007) 1976.
- [15] V.T. Kavitha, R. Jose, S. Ramakrishna, P.R.S. Wariar, J. Koshy, Bull. Mater. Sci. 34 (2011) 661.
- [16] C.N. George, J.K. Thomas, R. Jose, H.P. Kumar, M.K. Suresh, V.R. Kumar, P.R.S. Wariar, J. Koshy, J. Alloys Compd. 486 (2009) 711.
- [17] C. Vijayakumar, H.P. Kumar, V.T. Kavitha, S. Solomon, J.K. Thomas, P.R.S. Wariar, J. Koshy, J. Alloys Compd. 475 (2009) 778.
- [18] H.P. Kumar, C. Vijayakumar, C.N. George, S. Solomon, R. Jose, J.K. Thomas, J. Koshy, J. Alloys Compd. 458 (2008) 528.
- [19] R. Ratheesh, H. Sreemoolanathan, M.T. Sebastian, J. Solid State Chem. 131 (1997) 2.
- [20] R. Sopracase, G. Gruener, E. Olive, J.C. Soret, Phys. B: Condens. Matter 405 (2010) 45.
- [21] A.E. Lavat, M.C. Grasselli, E.J. Baran, R.C. Mercader, Mater. Lett. 47 (2001) 194.
- [22] A. Corsmit, F.H.E. Hoefdraad, G. Blasse, J. Inorg. Nucl. Chem. 34 (1972) 3401.
- [23] C. Vijayakumar, H.P. Kumar, S. Solomon, J.K. Thomas, P.R.S. Wariar, A. John, J. Alloys Compd. 480 (2009) 167.
- [24] W. Zheng, W. Pang, G. Meng, Mater. Lett. 37 (1998) 276.
- [25] W. Kraus, G. Nolze, J. Appl. Crystallogr. 29 (1996) 301.
- [26] D.I. Woodward, I. Reaney, Acta Crystallogr. B 61 (2005).
- [27] R.D. Shannon, J. Appl. Phys. 73 (1994) 348.